

# Large-Eddy Simulation of Turbulent Flames in Syn-Gas Fuel-Air Mixtures

Baris A. Sen\* and Suresh Menon†

*School of Aerospace Engineering, Georgia Institute of Technology,  
Atlanta, GA, 30332-0150, USA*

Combustion characteristics of synthetic gaseous fuels ( $H_2$  and  $CO$  mixture) have been investigated in laminar and turbulent flow configurations with special emphasis on flame structure and propagation characteristics of  $CO$ -rich and  $H_2$ -rich premixed flames. Two reduced  $CO - H_2$  mechanisms (10-step and 5-step) are first investigated and it is shown that the 10-step mechanism is quite accurate over a wide range of equivalence ratios and with and without  $CO_2$  dilution. The 10-step mechanism is then used for both laminar and turbulent premixed flame calculations of both  $CO$ -rich and  $H_2$ -rich mixtures. The effect of a single isolated vortex interacting with a laminar flame and of a pair of counter rotating vortices with a turbulent premixed flame front are investigated for different turbulence levels. It is shown that  $H_2$  reaction zone is much thinner than the  $CO$  reaction zone, and that they do not overlap physically. Under certain conditions, the  $H_2$  reaction rate contours can become broken even when the  $CO$  reaction rate contours remains contiguous. Flame structure and propagation (burning) speed are substantially different depending upon the syn-gas ( $CO - H_2$ ) composition. Flame-vortex interaction creates large-scale flame wrinkling, the scale of which also depends on the initial fuel composition. Flame-vortex interactions also causes local enhancement and dissipation of vorticity depending on the local baroclinic torque and dilatation effects.

## I. Introduction

Energy production via converting chemical energy into mechanical energy by combustion processes rely heavily on hydrocarbon fuels and more specifically natural gas.<sup>1</sup> Although it has widespread usage especially in gas turbine engines, in recent years environmental concerns have prompted consideration of alternative fuel sources such as synthetic gas. Synthetic gas is a term used to describe the mixture that is produced during the formation of gaseous hydrogen from processed hydrocarbon fuels.<sup>2</sup> Also, it is mainly used by Integrated Gasification Combined Cycle (IGCC) systems in order to reduce the high amount of  $CO_2$  released to the atmosphere by coal power plants. In an IGCC system, the coal is not burned directly but rather is partially oxidized at high pressures through gasifier, which produces syngas mostly composed of  $CO$  and  $H_2$ . A report by Bradar, *et.al.*<sup>3</sup> indicates that General Electrics has 17 IGCC projects ranging from 12 MW up to 550 MW, where half of these projects are in operation accumulating over 250000 fired hours of synthetic gas experience. Coal based synthetic fuels may provide a way to reduce global demand for oil, lowering its cost and decreasing global dependence on Middle East petroleum.<sup>4</sup>

Flow features occurring inside industrial gas turbine combustors have been studied in details by many research groups, especially for natural gas fuels.<sup>5-8</sup> However, combustion characteristics of synthetic gaseous fuels, especially flame stabilization and local extinction processes are not well known and have to be studied further. The objective of this paper is to examine the combustion of synthetic gaseous fuels for different fuel compositions and turbulence levels. This is accomplished by Direct Numerical Simulation (DNS) for laminar and Large Eddy Simulation (LES) for turbulent flow configurations using the following benchmark cases:

---

\*Graduate Research Assistant, AIAA Student Member.

†Professor, AIAA Associate Fellow.

(i) one dimensional propagation of a premixed mixture on a channel, (ii) laminar flame-vortex interaction (FVI)<sup>9-11</sup> and (iii) flame-turbulence interaction (FTI).<sup>12-15</sup> The analysis reported below will focus on flame-vortex interaction as a function of  $CO - H_2$  composition and inflow turbulence level.

## II. Mathematical Formulation

### II.A. LES Modeling

Simulations of both laminar and turbulent flame-vortex interactions are studied using the same numerical method and solver. For turbulent simulations a LES approach with a subgrid mixing and combustion model is employed. The fully compressible, unsteady, multi-species Favre-filtered Navier Stokes equations for continuity, momentum, total energy and species conservation are:

$$\begin{aligned}
\frac{\partial \bar{\rho}}{\partial t} + \frac{\partial \bar{\rho} \tilde{u}_i}{\partial x_i} &= 0 \\
\frac{\partial \bar{\rho} \tilde{u}_i}{\partial t} + \frac{\partial}{\partial x_j} [\bar{\rho} \tilde{u}_i \tilde{u}_j + \bar{p} \delta_{ij} - \bar{\tau}_{ij} + \tau_{ij}^{sgs}] &= 0 \\
\frac{\partial \bar{\rho} \tilde{E}}{\partial t} + \frac{\partial}{\partial x_i} [(\bar{\rho} \tilde{E} + \bar{p}) \tilde{u}_i + \bar{q}_i - \tilde{u}_j \bar{\tau}_{ji} + H_i^{sgs} + \sigma_{ij}^{sgs}] &= 0 \\
\frac{\partial \bar{\rho} \tilde{Y}_k}{\partial t} + \frac{\partial}{\partial x_i} [\bar{\rho} \tilde{Y}_k \tilde{u}_i - \bar{\rho} \tilde{D}_k \frac{\partial \tilde{Y}_k}{\partial x_j} + \phi_{i,k}^{sgs} + \theta_{i,k}^{sgs}] &= \bar{\omega}_k
\end{aligned} \tag{1}$$

Here,  $\sim$  represents Favre averaging operator and is calculated for a given quantity  $\tilde{f}$  as  $(\bar{\rho} f / \bar{\rho})$ , where the overbar stands for spatial filtering using a top-hat filter. The terms (denoted by superscript  $sgs$ ) in the LES equations require closure and are the subgrid shear stress:  $\tau_{ij}^{sgs} = \bar{\rho} [\widetilde{u_i u_j} - \tilde{u}_i \tilde{u}_j]$ , the subgrid enthalpy flux:  $H_i^{sgs} = \bar{\rho} [\widetilde{E u_i} - \tilde{E} \tilde{u}_i] + [\widetilde{p u_i} - \bar{p} \tilde{u}_i]$ , the subgrid viscous work:  $\sigma_{ij}^{sgs} = [\widetilde{u_j \tau_{ji}} - \tilde{u}_i \bar{\tau}_{ji}]$ , the subgrid mass flux:  $\phi_{jm}^{sgs} = \bar{\rho} [\widetilde{Y_m u_j} - \tilde{Y}_m \tilde{u}_j]$ , and the subgrid diffusive flux:  $\theta_{jm}^{sgs} = \bar{\rho} [\widetilde{Y_m V_{j,m}} - \tilde{Y}_m \tilde{V}_{j,m}]$ . Total energy is given as  $\tilde{E} = \tilde{e} + \frac{1}{2} \tilde{u}_k \tilde{u}_k + k^{sgs}$ , where  $\tilde{e}$  is the filtered internal energy,  $k^{sgs}$  is subgrid scale kinetic energy. The filtered pressure is calculated by the filtered equation of state by neglecting the effect of the subgrid scale temperature as  $\bar{p} = \bar{\rho} R \bar{T}$ , where  $R$  is the mixture gas constant.

For momentum and energy transport, the major effect of the small scales is to provide dissipation for the energy cascade from large scales. Therefore, an eddy viscosity type subgrid model is suitable for the calculation of subgrid stresses,  $\tau_{ij}^{sgs}$  and enthalpy flux,  $H_i^{sgs}$ . In this study, the subgrid scale eddy viscosity is calculated as  $\nu_t = C_\nu (k^{sgs})^{\frac{1}{2}} \bar{\Delta}$ , where  $\bar{\Delta}$  is the grid cut-off scale. An additional transport equation for the subgrid scale kinetic energy  $k^{sgs}$  is solved, which is in the form of:

$$\frac{\partial \bar{\rho} k^{sgs}}{\partial t} + \frac{\partial}{\partial x_i} (\bar{\rho} \tilde{u}_i k^{sgs}) = P^{sgs} - D^{sgs} + \frac{\partial}{\partial x_i} \left( \frac{\bar{\rho} \nu_t}{Pr_t} \frac{\partial k^{sgs}}{\partial x_i} \right) \tag{2}$$

Here  $P^{sgs} = -\tau_{ij}^{sgs} \frac{\partial \tilde{u}_i}{\partial x_j}$  represents the production term, and  $D^{sgs} = C_\epsilon \bar{\rho} \frac{(\tilde{k}^{sgs})^{\frac{3}{2}}}{\bar{\Delta}}$ , is the dissipation term. The subgrid scale terms are closed as  $\tau_{ij}^{sgs} = -2\bar{\rho} \nu_t (\tilde{S}_{ij} - \frac{1}{3} \tilde{S}_{kk} \delta_{ij}) + \frac{2}{3} \bar{\rho} k^{sgs} \delta_{ij}$ , and  $H_i^{sgs} = -\bar{\rho} \frac{\nu_t}{Pr_t} \frac{\partial \tilde{H}}{\partial x_i}$ . Here,  $Pr_t = 1$  and the two coefficients,  $C_\nu$  and  $C_\epsilon$  have constant value of 0.067 and 0.916, based on earlier calibration.<sup>16</sup> Also based on earlier studies, the subgrid viscous work,  $\sigma_{ij}^{sgs}$  is neglected for the current LES.

### II.B. Subgrid Combustion Modeling

The subgrid mass flux,  $\phi_{jm}^{sgs}$ , the subgrid diffusive flux  $\theta_{jm}^{sgs}$ , and the filtered reaction rate  $\bar{\omega}_k$  all require closure as well. However, a closure at the resolved scale (as done for momentum and energy transport) is not appropriate since combustion, heat release, volumetric expansion and small-scale turbulent stirring all occur at the small scales, which are not resolved in a conventional LES approach. To address this important physics, in our study a subgrid combustion model based on the Linear Eddy Mixing (LEM)<sup>17</sup> model is used to model combustion occurring within every LES cells (called LEMLES, hereafter). With this approach,

there is no need to provide explicit closure for  $\phi_{jm}^{sgs}$ ,  $\theta_{jm}^{sgs}$ , and  $\bar{\omega}_k$  since a more accurate and exact closure is implemented within the subgrid scales. LEMLES methodology and its ability has been reported extensively elsewhere,<sup>18-20</sup> however, for completeness we give a brief overview of the methodology below.

Consider the following exact transport equation for the  $k$ th scalar  $Y_k$ , where there is no LES filtering:

$$\rho \frac{\partial Y_k}{\partial t} = -\rho[\tilde{u}_i + (u'_i)^R + (u'_i)^S] \frac{\partial Y_k}{\partial x_i} - \frac{\partial}{\partial x_i} (\rho Y_k V_{i,k}) + \dot{\omega}_k \quad (3)$$

In the above equation,  $V_{i,k}$  is the  $k$ -th species diffusion velocity that is obtained using Fick's law. To describe the LEMLES approach, the convective velocity is separated into three parts as:  $\tilde{u}_i + (u'_i)^R + (u'_i)^S$  that represent respectively, the LES resolved velocity field, the LES resolved subgrid fluctuation (obtained from  $k^{sgs}$ , and the unresolved subgrid fluctuation. Using this definition, Eq. (3) can be recast into the following two-step numerical form:<sup>20</sup>

$$\frac{Y_k^* - Y_k^n}{\Delta t_{LES}} = -[(\tilde{u}_i + u'_i)^R] \frac{\partial Y_k^n}{\partial x_i} \quad (4)$$

$$Y_k^{n+1} - Y_k^* = \int -\frac{1}{\rho} [\rho (u'_i)^S \frac{\partial Y_k}{\partial x_i} + \frac{\partial}{\partial x_i} (\rho Y_k V_{i,k})^n - \dot{\omega}_k] dt' \quad (5)$$

Here, Eqs. (4) and (5) represent large-scale and small-scale processes, respectively, and  $\Delta t_{LES}$  is the LES time step. The large-scale step advects the subgrid scalar gradient using a 3D Lagrangian process that ensures strict mass conservation and preserves the small-scale scalar structure. Within each LES cell the subgrid scale processes (the integrand in Eq. (5)) represent respectively, the small-scale turbulent stirring, molecular diffusion and reaction kinetics. The integrand is solved on a 1D line embedded inside each LES cells with a subgrid resolution that is fine enough to resolve the Kolmogorov scale,  $\eta$ . With such a resolution, both molecular diffusion and reaction rate are closed in an exact sense and this is one of the major strengths of the LEMLES strategy. The 1D line is aligned in the flame normal or the maximum scalar gradient direction and thus, does not represent any physical Cartesian direction. More specifically, the following reaction-diffusion equation (and an accompanying energy equation) is solved on the 1D LEM line for species mass fraction:

$$\rho \frac{\partial Y_k^m}{\partial t^s} = F_s^m - \frac{\partial}{\partial s} (\rho Y_k^m V_{s,k}^m)^n + \dot{\omega}_k^m \quad (6)$$

Here  $t^s$  indicates a local LEM timescale and the superscript  $m$  indicates that the subgrid field within each LES supergrid is resolved by  $N_{LEM}$  number of LEM cells (i.e.,  $m = 1, 2, \dots, N_{LEM}$ ) along the local coordinate  $s$  (which is aligned in the direction of the steepest gradient).

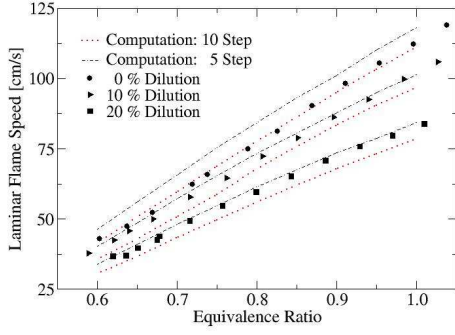
In the above equation, turbulent stirring is represented by  $F_s^m$  and is implemented using a stochastic re-arrangement events that stir the subgrid scalar fields within each LES cell. The location of stirring event is chosen from a uniform distribution and the frequency of stirring is derived from 3D inertial range scaling laws derived from Kolmogorov's hypothesis as:<sup>21</sup>

$$\lambda = \frac{54 \nu Re_{\bar{\Delta}} [(\frac{\bar{\Delta}}{\eta})^{\frac{5}{3}} - 1]}{5 C_{\lambda} \bar{\Delta}^3 [1 - (\frac{\eta}{\bar{\Delta}})^{\frac{4}{3}}]} \quad (7)$$

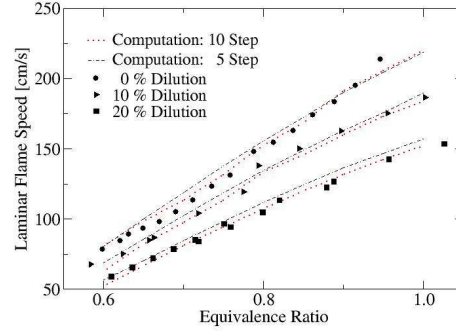
where,  $C_{\lambda} = 0.067$ .<sup>22</sup> The eddy size ( $l$ ) is picked randomly from an eddy size distribution  $f(l)$  ranging from  $\bar{\Delta}$  to  $\eta$ :  $f(l) = \frac{5}{3} \frac{l^{-\frac{8}{3}}}{\eta^{\frac{8}{3}} - \bar{\Delta}^{\frac{8}{3}}}$  where  $\eta = N_{\eta} \bar{\Delta} Re_{\bar{\Delta}}^{-3/4}$ ,  $N_{\eta} = 5^{23}$  and  $Re_{\bar{\Delta}} = u' \bar{\Delta} / \nu$  is the subgrid Reynolds number.

Volumetric expansion due to heat release is implemented locally within the subgrid by expanding the LEM domain. Although not required, re-gridding is employed to keep the total number of LEM cells constant throughout the simulation to reduce programmatic complexity. Re-gridding can introduce some numerical diffusion that is shown to be negligible in compressible flow simulations using an explicit time step  $\Delta t_{LES}$  (which is limited by acoustic time scale).

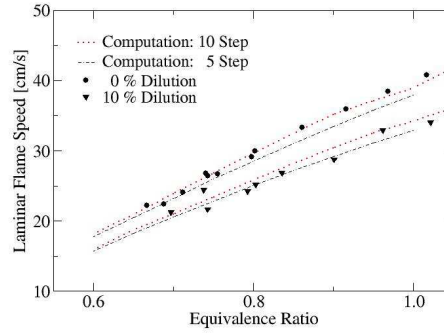
Once the subgrid evolution has occurred, large-scale advection (Eq. 4) is implemented by a 3D Lagrangian process that determines the amount of mass to be advected and explicitly advecting this amount (and



(a) 50:50  $H_2:CO$  with 0%, 10% and 20%  $CO_2$  dilution



(b) 95:5  $H_2:CO$  with 0%, 10% and 20%  $CO_2$  dilution



(c) 5:95  $H_2:CO$  with 0% and 10%  $CO_2$  dilution

Figure 1. Variation of laminar flame speed  $S_L$  with equivalence ratio and  $CO_2$  dilution

the accompanying subgrid scalar fields) across the LES cell faces. Further details of this process is given elsewhere.<sup>20</sup> Finally, the LES-filtered species mass fractions  $\tilde{Y}_k$  (used in the LES equations) are obtained by Favre averaging the subgrid mass fractions,  $Y_k^m$ :

$$\tilde{Y}_k = \left( \frac{1}{\sum \rho^m} \right) \sum (\rho Y_k^m)^m \quad (8)$$

### III. Results and Discussion

#### III.A. Evaluation of Reduced Chemical Kinetics Model

Laminar flame speeds associated with combustion of premixed synthetic gaseous fuel-air mixtures are calculated for different fuel compositions with two reduced mechanisms (10-step 14-species and 5-step 9-species). These reduced mechanisms are given in Appendix 1. Selected fuel compositions are (i) 50:50  $H_2:CO$  with 0%, 10%, 20%  $CO_2$  dilution, (ii) 95:5  $H_2:CO$  with 0%, 10% 20%  $CO_2$  dilution and (iii) 5:95  $H_2:CO$  with 0%, 10%  $CO_2$  dilution. Computations are performed using CHEMKIN PREMIX software, and the results are compared with some recent data.<sup>24</sup>

Fig. 1 shows that the laminar flame speed  $S_L$  increases with an increase in equivalence ratio  $\phi$  and

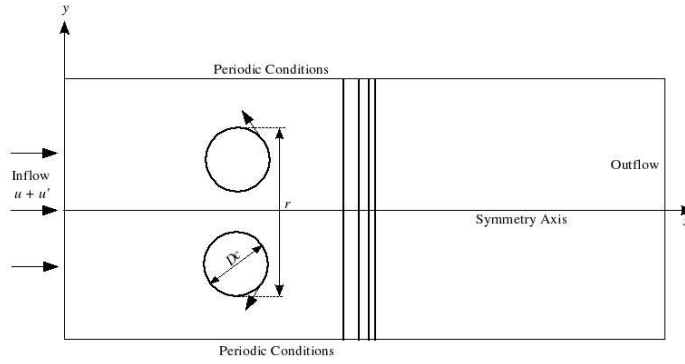


Figure 2. Schematics of the computational domain

$H_2$  content. For example, the laminar flame speed increases to around 200 cm/s for an equivalence ratio of approximately 0.93 in the 95:5  $H_2 : CO$  mixture (Fig. 1b).  $CO_2$  dilution decreases the laminar flame velocity for all fuel compositions. For example,  $S_L$  decreases to around 150 cm/s with a 20%  $CO_2$  dilution for this case. Increase in the  $CO$  content (at the expense of  $H_2$  content) also decreases  $S_L$ . For an equivalence ratio of 0.8,  $S_L = 80$  cm/s for 50:50  $H_2:CO$  fuel mixture (Fig. 1a) but it drops to 28 cm/s for a 5:95  $H_2:CO$  mixture (Fig. 1c). Hence, for a given equivalence ratio, the lowest laminar flame speed is obtained for  $CO$ -rich flame with  $CO_2$  dilution. In general, the agreement between the experimental and computational profiles is acceptable. The 10-step mechanism predicts the experimental data fairly well for both  $CO$ -rich and  $H_2$ -rich fuel composition at all dilution ratios. However, for 50:50  $H_2:CO$  fuel composition with an increased dilution rate the accuracy is not as good. Regardless, the accuracy of the 10-step reduced mechanism is considered overall acceptable, and therefore, we employ it for the rest of the study reported below.

### III.B. Flame-Vortex Interaction

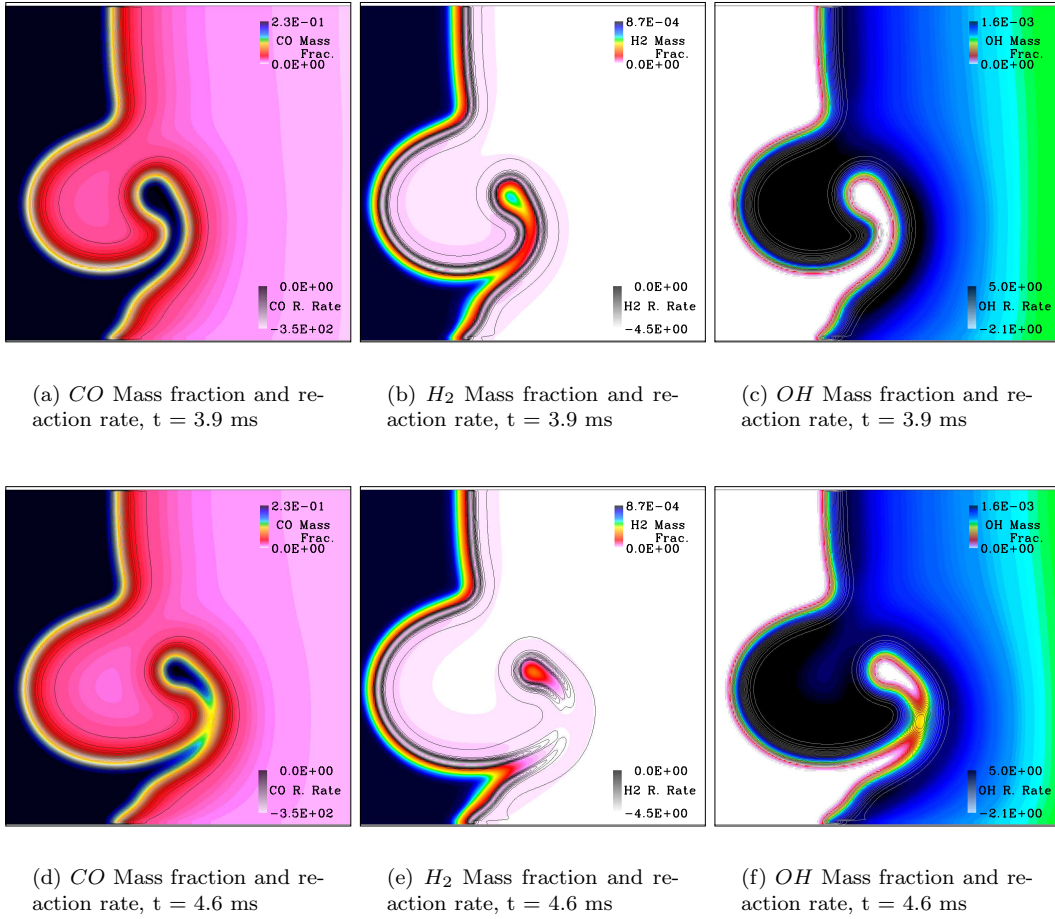
Effect of the syngas fuel composition on the flame-vortex interactions is investigated under laminar conditions using the 10-step  $CO - H_2$  reduced mechanism. Figure 2 (without the inflow turbulence) schematically shows this set-up. The initial vortex is generated using an analytical model (given below) and two cases with different fuel compositions are simulated. Table 1 summarizes the test cases.

Table 1. Parameters for laminar flame-vortex interaction simulations

	$S_L$ [m/s]	$u_{c,max}$ [m/s]	$l_f$ [m]	$D_c$ [m]	Fuel
FVI-Case 1	0.2457	2.4819	0.000898	0.002694	5:95 $H_2:CO$
FVI-Case 2	1.9032	19.2230	0.00033	0.00099	95:5 $H_2:CO$
FVI-Case 3	0.1156	1.1680	0.00099	0.00297	100 $CH_4$

Here,  $u_{c,max}$ ,  $D_c$  and  $l_f$  are the maximum velocity induced by the vortex, the initial vortex diameter and the laminar flame thickness, respectively. FVI-Case 1 is  $CO$ -rich whereas FVI-Case 2 is  $H_2$ -rich. FVI-Case 3 is a methane case simulated earlier<sup>2</sup> and is not discussed here but is shown for reference purpose only. The equivalence ratio is selected to be 0.6 for both cases. The flow field inside the computational domain is initialized by the output obtained from PREMIX code. Following an earlier DNS study,<sup>9</sup> two counter rotating vortices are created at  $t = 0$  s on the upstream side of a laminar flame front. As the flow is symmetrical with respect to the  $x$  axis, only the upper part is calculated. The inlet flow speed is equal to the laminar flame speed so that the flame does not move when it is not perturbed. The velocity field corresponding to each vortex is initialized using the stream function ( $\psi$ ) for an incompressible non-viscous vortex:

$$\begin{pmatrix} u \\ v \end{pmatrix} = \begin{pmatrix} u_0 \\ v_0 \end{pmatrix} + \frac{1}{\rho} \begin{pmatrix} \frac{\partial \psi}{\partial y} \\ -\frac{\partial \psi}{\partial x} \end{pmatrix} \quad (9)$$



**Figure 3. Evolution of  $CO$ ,  $H_2$ ,  $OH$  mass fraction and reaction rate for FVI-Case 1**

$$\psi = C \exp\left[\frac{-(x_0^2 + y_0^2)}{2R_c^2}\right] \quad (10)$$

Here,  $C$  determines the vortex strength,  $R_c$  is the vortex radius, and  $x_0, y_0$  are the distance to the center of the core of the vortices. Since  $S_L$  and  $l_f$  of each fuel mixture is different, to reproduce similar type of flame-vortex interaction regardless of the type of the fuel, the ratios  $u_{c,max}/S_L = 10.1$  and  $D_c/l_f = 3.1$  for both cases. These values were identified as a strong vortex case in an experimental FVI study<sup>25</sup> using propane as the fuel. For the current simulations, a 2D uniform grid of  $512 \times 192$  is employed to resolve a domain with a non-dimensional length ( $L/l_f$ ) and height ( $H/l_f$ ) of 61 and 23, respectively. For this resolution, the flame thickness is resolved with 9 grid points in all cases.

Evolution of  $CO$ ,  $H_2$ , and  $OH$  reaction rate and mass fraction are shown in Fig. 3 at two time instants;  $t = 3.9$  and  $4.6$  ms during the flame-vortex interaction process. At these instants the vortex has passed through the flame and caused a large-scale wrinkling of the flame structure and size of the vortex is considerably reduced during this process. Since,  $H_2$  is a light species, it diffuses much more rapidly than  $CO$ .  $H_2$  is also consumed earlier and the  $H_2$  reaction rate is concentrated in a thinner region when compared to the  $CO$  reaction rate contours. The  $H_2$  reaction rate contours are also located slightly ahead of the  $CO$  reaction rate contours. The  $OH$  mass fraction, being an intermediate species, increases across the flame front and then decreases towards the downstream. Similar to  $CO$ ,  $OH$  reaction rate covers a wide area across the flame. Although not strictly valid, here and in the subsequent discussions we use the  $H_2$  and the  $CO$  reaction rate contours to locate their respective “flame” locations.

Vortex induced stretching and increased curvature of the initial planar laminar flame is clearly seen in

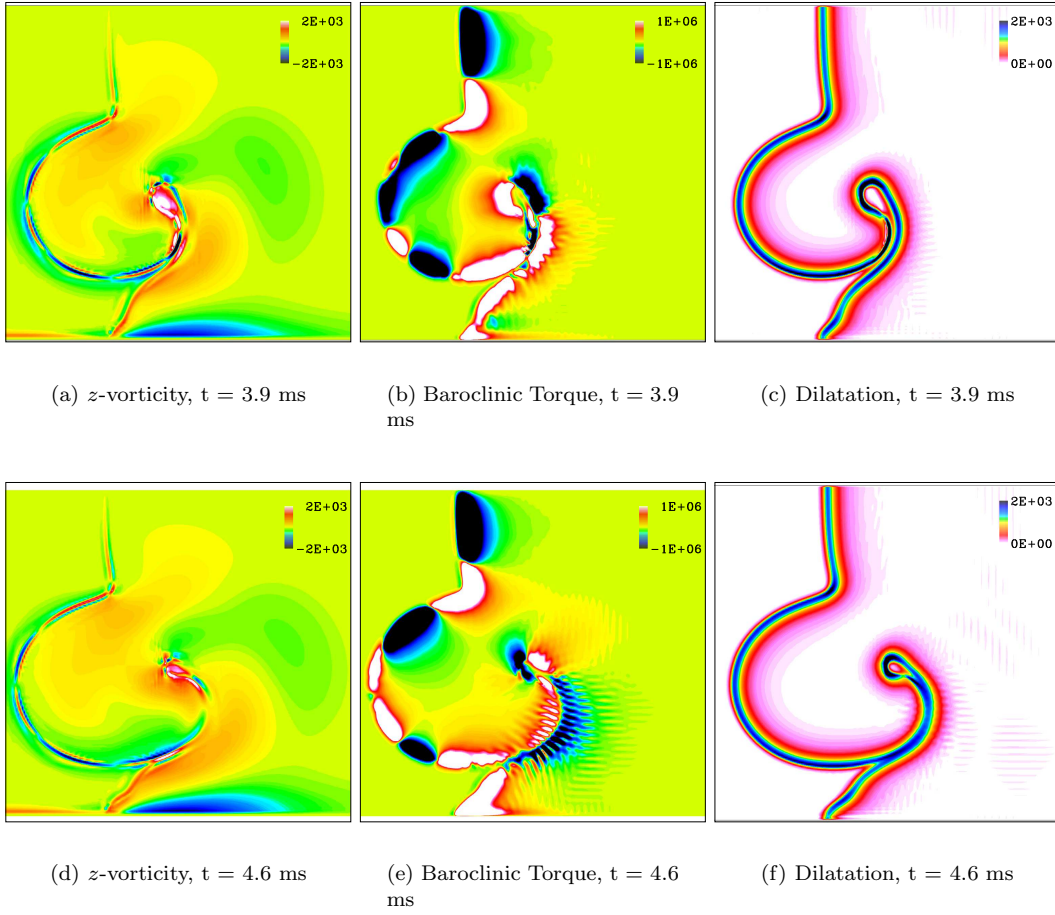


**Figure 4. Evolution of  $z$ -vorticity Baroclinic Torque and Dilatation for FVI-Case 1**

these figures. It can also be seen that at the later time a discontinuity in the  $H_2$  reaction rate contours occurs due to this stretching effect. Although  $H_2$  reaction rate contours show a separated pocket of  $H_2$  burning,  $CO$  reaction rate contours still shows a continuous region in regions where no  $H_2$  reaction rate. This is also apparent in  $OH$  reaction rate plot and suggests that the overall flame structure is still unbroken although the reactions and hence, the heat release are no longer same at all locations along the flame. Although not yet investigated, this variability is likely to be a function of  $\phi$ ,  $u_{c,max}/S_L$  and  $D_c/l_f$  values for a given fuel composition.

Additional insight into flame-vortex interaction can be obtained by evaluating the various mechanisms for vorticity generation and dissipation. For this we consider the vorticity transport equation:

$$\frac{\partial \vec{\omega}}{\partial t} + \vec{u} \cdot \nabla \vec{\omega} = (\vec{\omega} \cdot \nabla) \vec{u} + \nu \nabla^2 \vec{\omega} - \vec{\omega} (\nabla \cdot \vec{u}) + \frac{1}{\rho^2} (\nabla \rho \times \nabla P) \quad (11)$$

Here, the terms on the right hand side represent respectively, the vortex stretching, the viscous diffusion term, the dilatation and the baroclinic torque terms. For the current 2D study, there is only one component of vorticity ( $z$ -vorticity) and baroclinic torque terms and there is no vortex stretching term. In the flame normal direction, volumetric expansion (and hence, dilatation) is positive since gas velocity increases across the flame. The mixture density, on the other hand, always decreases across the flame due to heat release but the local pressure gradient can vary depending upon the local conditions. Heat release and increased viscosity due to temperature rise will also dissipate vorticity, although in this case since the initial vortex strength is strong this dissipation effect will take some time to occur. When the flame is non-planar, as in

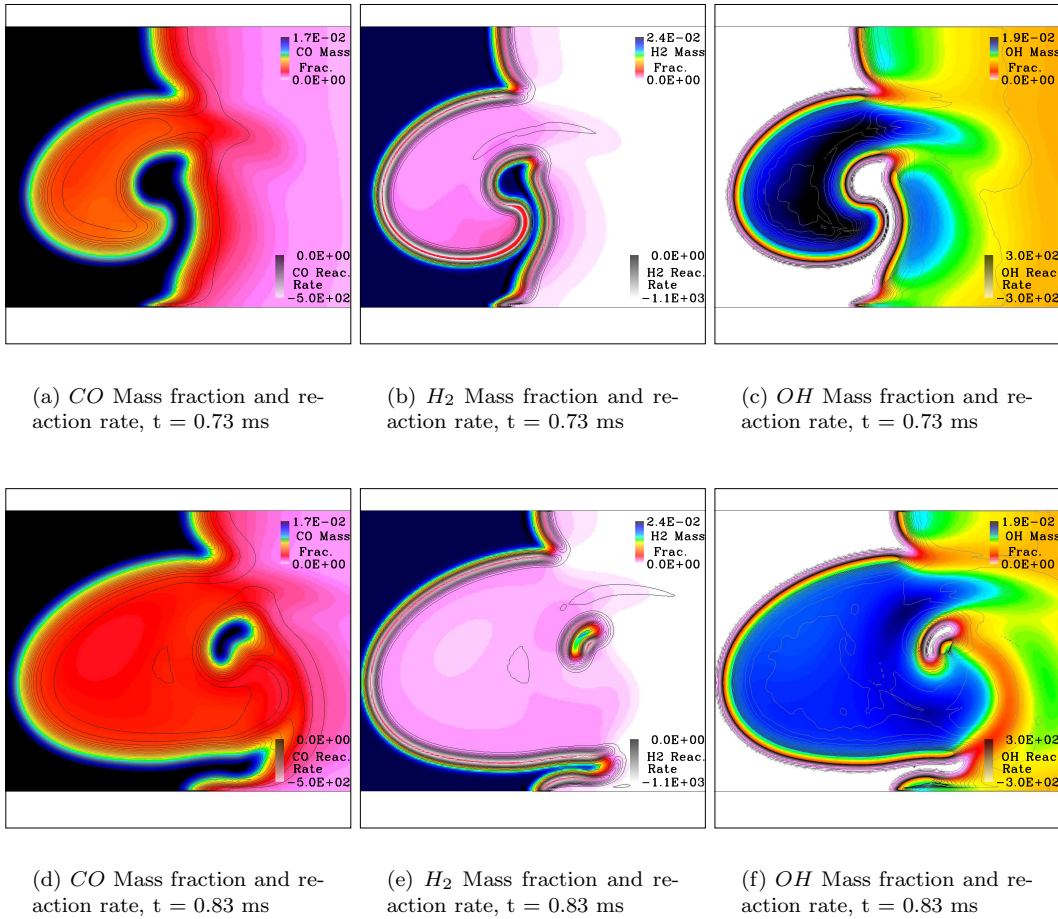
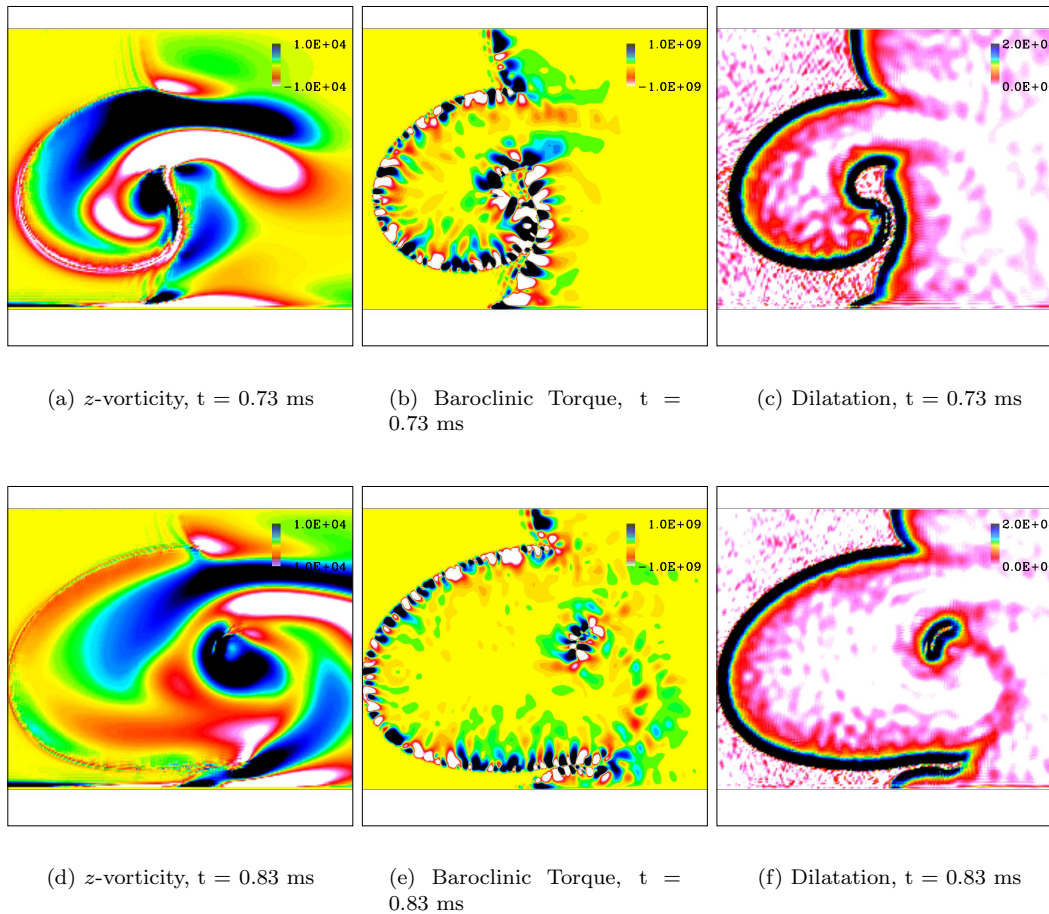


Figure 5. Evolution of *CO*,  $H_2$ , *OH* mass fraction and reaction rate for FVI-Case 2

cases simulated here, all these terms will show both positive and negative values in the plane of the flame.

Figure 4(a)-(c) show respectively, the  $z$ -vorticity, the baroclinic torque and the dilatation fields at the same two instants discussed earlier for the FVI-Case 1. As can be seen baroclinic torque show both positive and negative values along the flame, and their locations and magnitude depends on the stage of vortex-flame interactions. Baroclinic torque in this Fig. 4 (b) mostly attains positive values in the region where the vortex interacts with the flame. The dilatation attains its peak values at the neck region, tip of the pocket formation region and at the region where the flame is convex towards the reactants, indicating maximum rate of dissipation occurs at these locations. Except for the neck region, the baroclinic torque is also positive balancing the effect of dilatation. At later stages both dilatation and baroclinic torque loses their strength especially on the region where vortex interacts with the flame. The part of the flame which is convex to the reactants will be referred as a region having negative curvature hereafter. The negative curvature region is a possible source for the generation of vorticity as shown in Fig. 4 (a) and (d). The portion of the flame which is rotated in counter clock wise exhibits mostly negative baroclinic torque on the upper half region inhibiting extension of vorticity to these regions. On the other hand, the negatively curved region close to the upper boundary exhibits negative baroclinic torque values. For this, case there is flame generated vorticity (FGV) but apparently not sufficient enough to cause any flame quenching.

The corresponding *CO*,  $H_2$ , and *OH* mass fraction and reaction rate contours for the FVI-Case 2 are shown in Fig. 5 at two time instants. Since this is a  $H_2$ -rich mixture, flame propagation is substantially faster than in FVI-Case 1 and therefore, the flame-vortex interaction occurs much more rapidly, and this is reflected in the time instants. As in FVI-Case 1, mass fraction and reaction rate of *CO* exist over a larger



**Figure 6. Evolution of  $z$ -vorticity, Baroclinic Torque and Dilatation for FVI-Case 2**

region compared to  $H_2$  due to its lower diffusivity and slower reaction rate. The  $H_2$  reaction rate contours are not continuous and pocket burning is seen. Compared to Fig. 3, the length of the flame front has increased and the curvature is larger. This is related to faster burning speed for this mixture. For this case the  $CO$  and  $OH$  reaction rates are also discontinuous at both of the negatively curved regions. The  $OH$  mass fraction seem to be trapped within the counter clock wise rotated portion of the flame.  $CO$  is relatively in low concentration compared to  $H_2$ , but still shows some presence in the flame front. However, the reaction rate in the neck region do not indicate a high rate of burning at this region.

Figures 6(a)-(c) show respectively, the  $z$ -vorticity, baroclinic torque and dilatation for this case. Lighter species diffusion takes place faster compared to FVI-Case 1 and as a result, flame has an increased sensitivity to the initial vortex size/strength. Overall flame length is much larger for this case as well. Unlike FVI-Case 1 baroclinic torque does not seem to get clear distribution along the flame front but rather attains alternating positive and negative values except for two negatively curved regions: the region where the flame wraps the vortex and the region close to the upper boundary. Considerable amount of vorticity seem to be generated at these locations and they tend to extend through downstream as shown both in Fig. 6 (a) and (d). Dilatation term seem to obtain high values along the flame and seem to be not affecting the region where there is vorticity generation. As both these negatively curved regions approach each other, the baroclinic torque attains alternating values similar to the distribution on rest of the flame and the the vorticity that was generated on these regions seem to be getting weak as shown in the vorticity plot.

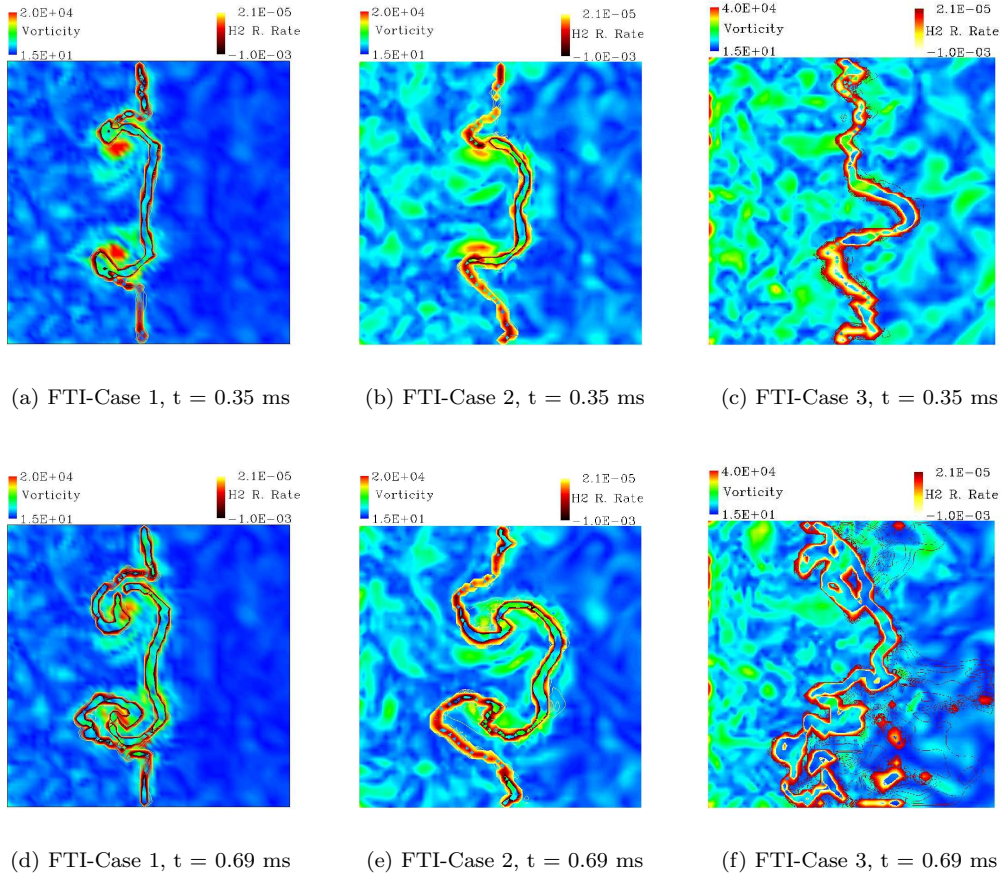


Figure 7. Evolution of  $H_2$  reaction rate and  $z$ -vorticity

### III.C. Flame-Turbulence Interaction

Table 2. Simulation parameters for flame turbulence interaction problem

	$u'/S_L$	$D_c/l_f$	$Re\lambda$	Regime [m]	Box Size [cm]
FTI-Case 1	10	5	38.13	TRZ	3.0
FTI-Case 2	5	5	26.96	TRZ	5.0
FTI-Case 3	30	5	66.04	BRZ	2.5

Flame-turbulence interaction is studied using LEMLES with an embedded vortex sheet to understand how large scale vortices can stretch turbulent flames that are wrinkling both by large and small scales. Figure 2 shows the schematic of this test case. We consider a flame front interacting with a pair of spanwise vortices superimposed on an isotropic turbulent premixed mixture.  $u_c, max/S_L$  and  $D_c/l_f$  for this vortex pair is 50 and 5, respectively. The fuel composition and the size of the coherent structure are held constant, and 3 different background turbulence levels are simulated. The turbulent levels are chosen such that for the equivalence ratio, the resulting  $u'/S_L$  makes the flame to be in the thin-reaction-zone (TRZ) regime for FTI-Case 1 and FTI-Case 2, and in the broken-reaction-zone (BRZ) regime for FTI-Case 3. A  $64^3$  grid is used for all cases and the size of the computational domain is selected as to yield a minimum spacing of 3.3 times the Kolmogorov length scale. In the subgrid within each LES cell, 12 LEM cells ( $N_{LEM} = 12$ ) are used, which allows a resolution of 4 times smaller than  $\eta$ . The fuel composition is selected similar to

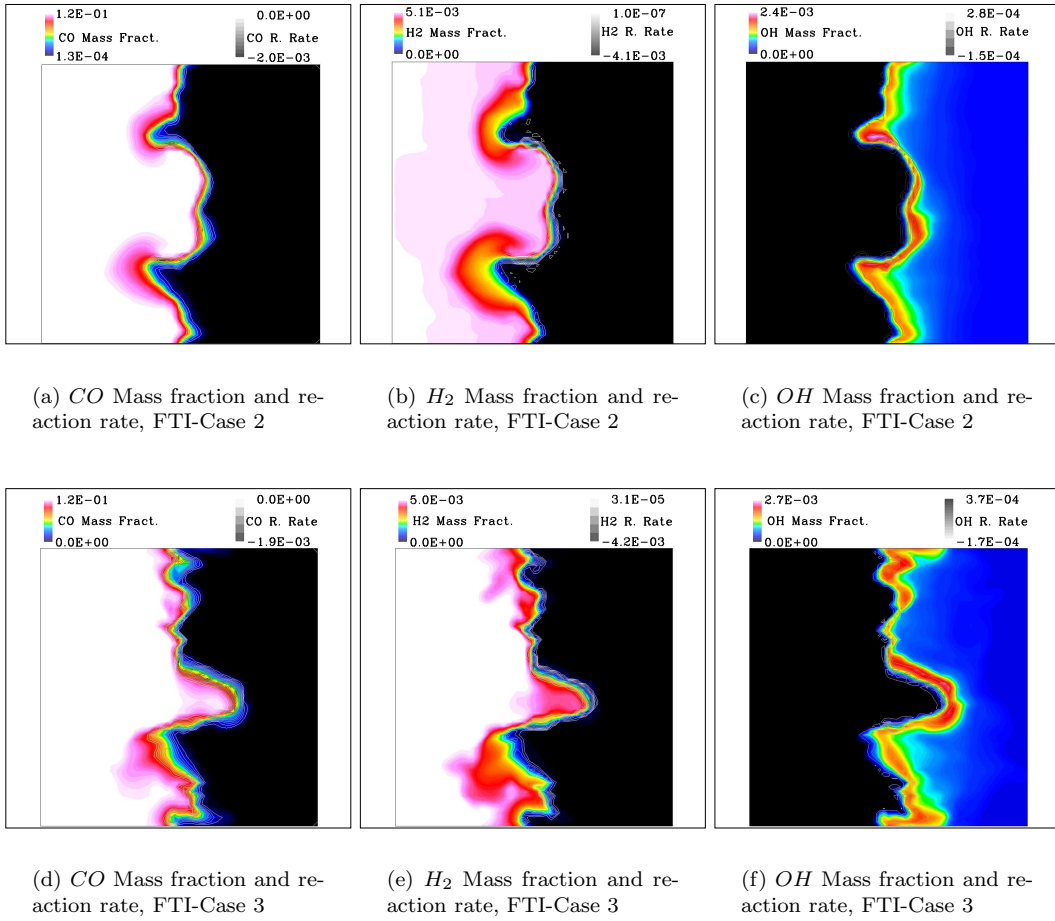


Figure 8. Evolution of  $CO$ ,  $H_2$ ,  $OH$  mass fraction and reaction rate at  $t=0.35$  ms

fuel composition PSI as defined by General Electric.<sup>3</sup> Simulation parameters and flame properties for FTI computations are summarized in Tables 2 and 3, respectively.

Evolution of the flame surface at two time instants for the three cases are given in Fig. 7. Similar to the laminar case, flame front is stretched and curved by the vortex pair, but the strength of these vortices decreases much more rapidly across the flame. The small-scale vorticity in the incoming turbulent field dissipates across the flame and only large scale structures exist in the burned side, with only FTI-Case 3 showing that largest scales more clearly. The vortices cause large scale wrinkling of the flame front as seen earlier in the laminar case. The flame front wrinkling increases with an increase in  $u'/S_L$  (from Case 1 to Case 3) and in Case 3 the flame structure (as identified by the  $H_2$  reaction rate) is much more distributed and broken compared to the TRZ cases. There is extensive flame front wrinkling caused by the large scale vortices and pocket formation similar to laminar FVI case. In these TRZ and BRZ regimes small scale structures can penetrate into the flame and increase the wrinkling effect. At the later time the BRZ case

Table 3. Flame Parameters used for flame turbulence interaction

	Fuel Composition	Equivalence Ratio	$S_L$ [m/s]	$l_f$ [m]
$H_2:CO:CO_2:H_2O$	0.0678:0.113:0.0254:0.0650	0.6	0.2105	$8.755 \times 10^{-4}$
$O_2:N_2$	0.1507:0.5781			

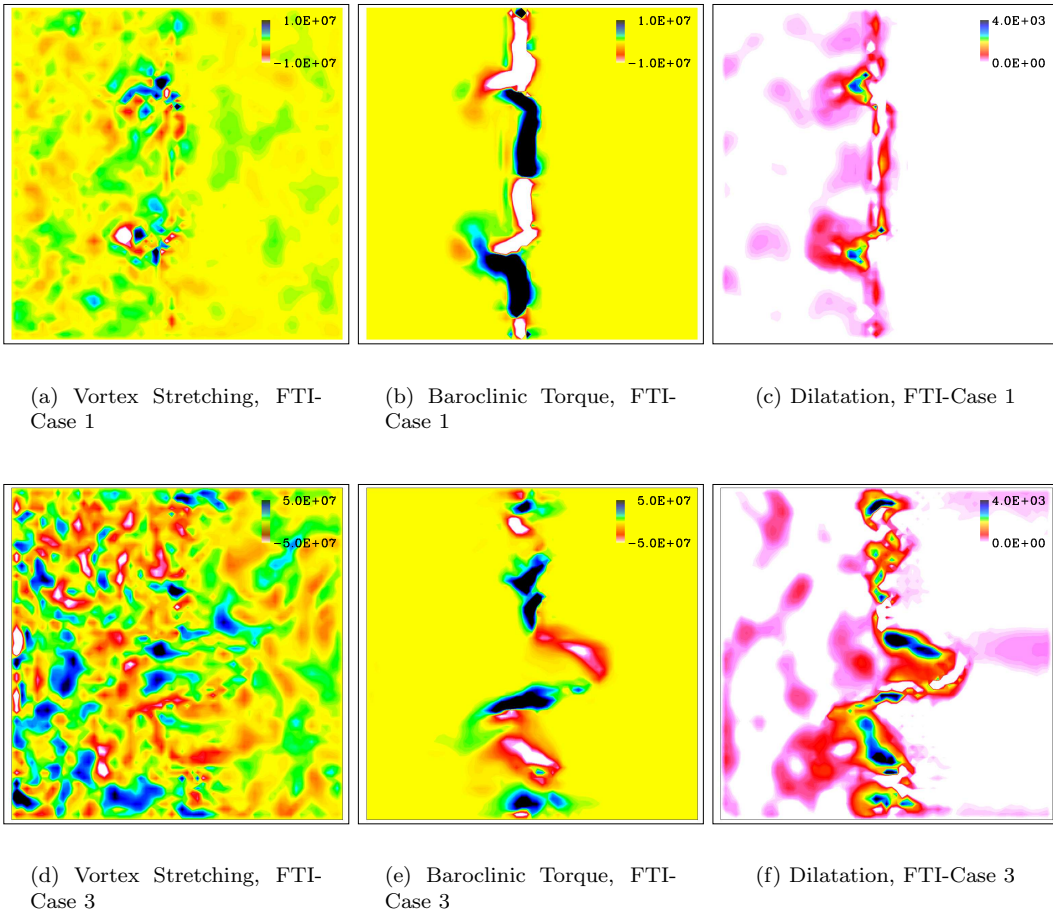


Figure 9. Evolution of  $z$  component of the Vortex Stretching, Baroclinic Torque and Dilatation at  $t = 0.35$  ms

shows broken region of reaction rate suggesting that the flame is no longer continuous.

In order to get a better insight into the effect of turbulence on the scalar field distribution,  $CO$ ,  $H_2$ , and  $OH$  reaction rate and mass fractions are plotted in Fig. 8 for FTI-Case 2 and 3. The  $CO$  consumption occurs over a wider region compared to  $H_2$  and the maximum reaction rate is attained on the thinner region of the flame surface. The  $H_2$  reaction rate exhibits very small or negligible values at several locations, including the stretched portion of the flame close to upper and lower boundaries of the computational domain. The  $CO$  reaction rate on the other hand, show finite reactions in these regions, again suggesting that the overall flame is still existing, albeit with significant variability in the plane of the flame. Both  $CO$  and  $H_2$  mass fractions exhibit lower gradients especially on the negatively curved portion of the flame, compared to the center part of the flame front. The situation is worse for  $H_2$  mass fraction and these low gradient regions tend to extend towards the upper and lower boundaries in  $y$  axis. The reaction rate of  $H_2$  also decreases in these parts of the flame and is discontinuous.  $CO$ , on the other hand and is not discontinuous, but still weak compared to the center part.  $OH$  mass fraction attains its maximum value on the center region due to the increased rate of fuel destruction occurring here.  $H_2$  reaction rate is occurring in a thin region compared to  $CO$ . In the positively curved region  $H_2$  reaction rate is enhanced and thus maximum amount of  $OH$  mass fraction is obtained in this location.

Fig. 9 show the vorticity, baroclinic torque and dilatation at  $t = 0.35$  ms for FTI-Case 1 and Case 3. The baroclinic torque for FTI-Case 1 seem to exhibit a clear distribution by changing its sign first at the negatively curved edge of the flame and then near the symmetry plane of  $y$  axis. The dilatation on the other hand is prominent only in a region that seem to match with the core of the coherent vortices. The

vortex stretching is also focused on the core region and is responsible for the attenuation of vortex pair in an early stage compared to FVI. For FTI-Case 2, the vortex stretching is prominent all over the computational domain since large scale structures for this case are almost at the same size and strength with the vortex pair of previous cases. Also, since the flame front exhibits interaction with many large scale structures, there is no clear distribution of the Baroclinic torque and dilatation.

## IV. Conclusion

The physics of the combustion of premixed synthetic gaseous flames are investigated by DNS and LES computations. The initial part of the study dealt with performing laminar flame velocity computations to validate the reduced chemical kinetics mechanisms that were used in the remaining part. Here, it was showed that the synthetic gaseous flames may correspond to a wide variety of laminar flame speeds based on the dilution rate and relative  $H_2$  to  $CO$  content of the fuel mixture. The motivation for the remaining sections of the study was to investigate the effect of different fuel compositions on flame dynamics by laminar FVI problems and to inspect how different turbulence levels changes the overall picture for the same fuel composition. For FVI computations it was observed that  $H_2$ , being a highly diffusive and reactive species, tend to exhibit a thinner reaction zone together with an early pocket formation process compared to  $CO$ . It appears that the  $CO$  reactions maintains the the flame in the highly stretched regions rather than  $H_2$ . Also, the flame front of a  $H_2$  rich syngas mixture was more susceptible to the flame wrinkling resulting in more vorticity generation.

The FTI computations showed that for a turbulent flow field the interaction between the coherent structures and the flame front was not as strong as it was suggested by laminar study. A decrease in the background turbulence level, increased the effect the coherent structures on the local flame dynamics. Turbulent eddies along the flame front induce local misalignments between pressure and density gradients causing more vorticity generation. The reaction rate of  $H_2$  and  $OH$  seem to be discontinuous especially in negatively curved flame regions. The vortex pair attenuates earlier composed to FVI computations since vortex stretching plays an important role for these cases.

## Acknowledgements

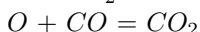
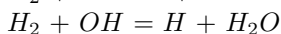
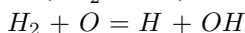
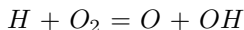
This work was supported in part by U.S. Department of Energy through a sub-contract from General Electric Corporate R & D division. The authors would like to acknowledge Prof. J.-Y. Chen for providing the reduced reaction mechanisms used in this study.

## Appendix

### IV.A. 5 Step reduced Chemical Kinetics Model

Species:  $H_2$ ,  $H$ ,  $O$ ,  $OH$ ,  $H_2O$ ,  $CO$ ,  $O_2$ ,  $CO_2$ ,  $N_2$

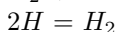
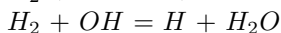
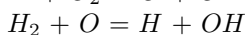
Reactions:

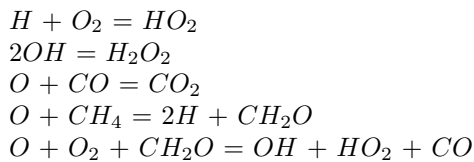


### IV.B. 10 Step reduced Chemical Kinetics Model

Species:  $H_2$ ,  $H$ ,  $O$ ,  $OH$ ,  $HO_2$ ,  $H_2O$ ,  $CO$ ,  $O_2$ ,  $H_2O_2$ ,  $CO_2$ ,  $CH_4$ ,  $CH_2O$ ,  $NO$ ,  $N_2$

Reactions:





## References

- <sup>1</sup>Turns, S. R., *An Introduction to Combustion*, McGraw-Hill, 2000.
- <sup>2</sup>Weiler, J., *Numerical Simulation of Flame-Vortex Interactions in Natural and Synthetic Gas Mixtures*, Master's thesis, Georgia Institute of Technology, Atlanta, USA, 2004.
- <sup>3</sup>Bradard, R. D. and Jones, R. M., "GE IGCC Technology and Experience with Advanced Gas Turbines," Ger-4207, GE Power Systems, Schenectady, NY, October 2000.
- <sup>4</sup>Hawkins, D. G., Lashow, D. A., and Williams, R. H., "What to do About Coal," *Scientific American*, september 2006, pp. 68–75.
- <sup>5</sup>Kempf, A., Lindstedt, R. P., and Janicka, J., "Large-eddy simulation of a bluff-body stabilized non-premixed flame," *Combust. Flame*, Vol. 144, 2006, pp. 170–189.
- <sup>6</sup>Eggenspieler, G. and Menon, S., "Structure of Locally Quenched Swirl Stabilized Turbulent Premixed Flames," *AIAA-2004-0979*, 2004.
- <sup>7</sup>Selle, L., Lartigue, G., Poinso, T., Koch, R., Schildmacher, K.-U., Krep, W., Prade, B., Kaufmann, P., and Veynante, D., "Compressible Large Eddy Simulation of Turbulent Combustion in Complex Geometry on Unstructured Meshes," *Combust. Flame*, Vol. 137, No. 1, 2004, pp. 489–505.
- <sup>8</sup>Menon, S., Stone, C., and Patel, N., AIAA 2004-0157, 2004.
- <sup>9</sup>Poinso, T., Veynante, D., and Candel, S., "Quenching processes and premixed turbulent combustion diagrams," *Journal of Fluid Mechanics*, Vol. 228, 1991, pp. 561–606.
- <sup>10</sup>Louch, D. S. and Bray, K. N. C., "Vorticity in Unsteady Premixed Flames: Vortex Pair-Premixed Flame Interactions Under Imposed Body Forces and Various Degrees of Heat Release and Laminar Flame Thickness," *Combust. Flame*, Vol. 125, 2001, pp. 1279–1309.
- <sup>11</sup>Roberts, W. L., Driscoll, J. F., Drake, M. C., and Goss, L. P., "Images of the Quenching of a Flame by a Vortex - To Quantify Regimes of Turbulent Combustion," *Combust. Flame*, Vol. 94, 1994, pp. 58–69.
- <sup>12</sup>Sankaran, V. and Menon, S., "Subgrid Combustion Modeling of 3-D Premixed Flames in the Thin-Reaction-Zone Regime," *Proc. Combust. Inst.*, Vol. 30, No. 1, 2005, pp. 575–582.
- <sup>13</sup>Chen, J. H., Echehki, T., and Kollmann, W., "The Mechanism of Two-Dimensional Pocket Formation in Lean Premixed Methane-Air Flames with Implications to Turbulent Combustion," *Combust. Flame*, Vol. 116, 1998, pp. 15–48.
- <sup>14</sup>Trouvé, A. and Poinso, T., "The Evolution Equation for the Flame Surface Density in Turbulent Premixed Combustion," *Journal of Fluid Mech.*, Vol. 278, 1994, pp. 1–31.
- <sup>15</sup>Baum, M., Poinso, T., Haworth, D. C., and Darabiha, N., "H<sub>2</sub>/O<sub>2</sub>/N<sub>2</sub> Flames with Complex Chemistry in Two-Dimensional Turbulent Flows," *J. Fluid Mech.*, Vol. 281, 1994, pp. 1 – 32.
- <sup>16</sup>Chakravarthy, V. and Menon, S., "Large-Eddy Simulations of Turbulent Premixed Flames in the Flamelet Regime," *Combust. Sci and Tech*, Vol. 162, 2000, pp. 1–48.
- <sup>17</sup>Kerstein, A. R., "Linear-Eddy Model of turbulent Scalar Transport and Mixing," *Combust. Sci. Tech.*, Vol. 60, 1988, pp. 391–421.
- <sup>18</sup>Menon, S., Yeung, P.-K., and Kim, W.-W., "Effect of Subgrid Models on the Computed Interscale Energy Transfer in Isotropic Turbulence," *Computers and Fluids*, Vol. 25, No. 2, 1996, pp. 165–180.
- <sup>19</sup>Eggenspieler, G. and Menon, S., "LES of Premixed Combustion and Pollutant Emission in a DOE-HAT Combustor," *AIAA-2003-0309*, 2003.
- <sup>20</sup>Menon, S. and Patel, N., "Subgrid Modeling for LES of Spray Combustion in Large-Scale Combustors," *AIAA Journal*, Vol. 44, No. 4, 2006, pp. 709–723.
- <sup>21</sup>Kerstein, A. R., "Linear-Eddy Model of Turbulent Transport II," *Combust. Flame*, Vol. 75, 1989, pp. 397–413.
- <sup>22</sup>Chakravarthy, V. and Menon, S., "Linear-Eddy Simulations of Reynolds and Schmidt Number Dependencies in Turbulent Scalar Mixing," *Physics of Fluids*, Vol. 13, 2001, pp. 488–499.
- <sup>23</sup>Smith, T. and Menon, S., "One-dimensional simulations of freely propagating turbulent premixed flames," *Combust. Sci. and Tech.*, Vol. 128, 1996, pp. 99–130.
- <sup>24</sup>Natarajan, J., Nandula, S., Lieuwen, T., and Seitzman, J., "Laminar Flame Speeds of Synthetic Gas Fuel Mixtures," *ASME Paper*, 2005.
- <sup>25</sup>Mueller, C. J., Driscoll, J. F., Reuss, D., and Drake, M., "Vorticity Generation and Attenuation as Vortices Convect Through a Premixed Flame," *Combust. Flame*, Vol. 112, 1998, pp. 342 – 358.